

The Shape of Galaxy Cluster Dark Matter Haloes: Systematics of Its Imprint on Cluster Gas, and Comparison to Observations

Ricardo A. Flores¹, Brandon Allgood², Andrey V. Kravtsov³, Joel R. Primack⁴, David A. Buote⁵, and James S. Bullock⁶

¹*Department of Physics and Astronomy, University of Missouri – St. Louis, St. Louis, MO 63121; ricardo.flores@umsl.edu*

²*Physics Department, University of California, Santa Cruz, CA 95064; allgood@physics.ucsc.edu*

³*Department of Astronomy and Astrophysics, Kavli Institute for Cosmological Physics, and The Enrico Fermi Institute, The University of Chicago, Chicago IL 60637; andrey@oddjob.uchicago.edu*

⁴*Physics Department, University of California, Santa Cruz, CA 95064; joel@scipp.ucsc.edu*

⁵*Department of Physics and Astronomy, University of California, Irvine, CA 92697; buote@uci.edu*

⁶*Center for Cosmology, Department of Physics and Astronomy, University of California, Irvine, CA 92697; bullock@uci.edu*

31 July 2021

ABSTRACT

We study predictions for galaxy cluster observables that can test the statistics of dark matter halo shapes expected in a flat Λ CDM universe. We present a simple analytical model for the prediction of cluster-scale X-ray observations, approximating clusters as isothermal systems in hydrostatic equilibrium, and dark matter haloes as ellipsoids with uniform axial ratios (homeoidal ellipsoids). We test the model against high-resolution, hydrodynamic cluster simulations to gauge its reliability. We find that this simple prescription does a good job of predicting cluster X-ray ellipticities compared to the simulations as long as one focuses on cluster regions that are less sensitive to recent mergers. Based on this simple model, the distribution of cluster-size halo shapes expected in the concordance Λ CDM cosmology implies an X-ray ellipticity distribution with a mean $\langle \epsilon_X \rangle = 0.32 \pm 0.01$, and a scatter $\sigma_\epsilon = 0.14 \pm 0.01$ for the mass range $(1 - 4) \times 10^{14} h^{-1} M_\odot$. We find it important to include the mass dependence of halo shape when making comparisons to observational samples that contain many, very massive clusters. We analyse the systematics of four observational samples of cluster ellipticities and find that our results are statistically compatible with observations. In particular, we find remarkably good agreement between two recent *ROSAT* samples and Λ CDM predictions that *do not* include gas cooling. We also test how well our analytical model can predict Sunyaev–Zel’dovich decrement maps and find that it is less successful although still useful; the model does not perform as well as a function of flux level in this case because of the changing triaxiality of dark matter haloes as a function of radial distance. Both this effect and the changing alignment of isodensity shells of dark matter haloes leave an imprint on cluster gas that appears to be seen in observational data. Thus, dark matter haloes cannot be accurately characterized as homeoidal ellipsoids for all comparisons.

Key words: cosmology: theory — dark matter — X-rays: galaxies: clusters

1 INTRODUCTION

Clusters of galaxies are the largest bound structures in the universe, and the most recently formed ones according to the very successful cold dark matter (CDM) cosmology. As such, their DM haloes are expected to be less evolved and more aspherical than, say, galaxy-size haloes. Most gas in

clusters DM haloes has not had time to cool, and since it is gravitationally subdominant, we can expect it to reflect the underlying 3D shape of their dark matter haloes. Indeed, large samples of X-ray clusters have been known to show a broad distribution of ellipticities in their surface brightness (SB) maps since the work of McMillan, Kowalski, & Ulmer (1989). A comparison of theoretical predictions to such ob-

servations, now that basic parameters of the underlying cosmology are known at the 10%–level or better, may shed light on the basic description of the gas in clusters of galaxies.

The general expectation that in CDM-based theories DM haloes are flattened, approximately ellipsoidal, and have short-to-long axial ratios as small as $s \equiv c/a \sim 0.5$ has been known for more than 15 years now (Barnes & Efstathiou 1987; Frenk et al. 1988). Any asphericity in the DM distribution has important effects on a variety of observed quantities. In clusters in particular, asphericity in the dark halo potential will map directly to asphericity in the gas density, and thus affect the shape of cluster X-ray isophotes and Sunyaev–Zel’dovich (SZ) isodecrement contours. Much subsequent work since these pioneering studies aimed at understanding the origin of such spatial anisotropy, the influence of the cosmological model on axial ratios, and improving the resolution with which the formation of DM haloes was followed (Dubinski & Carlberg 1991; Warren et al. 1992; Jing et al. 1995; Thomas et al. 1998; Suwa et al. 2003). Recently, higher resolution dissipationless simulations have made it possible to *fully characterize the scatter and mean of axial ratios*, as a function of both mass and epoch (Bullock 2002; Jing & Suto 2002; Kasun & Evrard 2004; Allgood et al. 2005). Jing & Suto (2002, hereafter JS) calculated for the first time axial ratios for isodensity shells, using cosmological simulations with 512^3 particles. They confirmed that haloes are approximately ellipsoidal in isodensity contours, and have provided fits for the dependence of axial ratios on mass and epoch. Because the isodensity contour method requires a large number of particles, JS restricted their analysis to haloes more massive than $6.2 \times 10^{12} h^{-1} M_\odot$ in their Λ CDM simulation. Kasun & Evrard (2004) have obtained better statistics for haloes more massive than $3 \times 10^{14} h^{-1} M_\odot$ from a Hubble volume simulation. We (Allgood et al. 2005, hereafter Paper I) have studied haloes spanning the mass range $4 \times 10^{11} - 2 \times 10^{14} h^{-1} M_\odot$ using several simulations to properly resolve and adequately sample the halo population in this entire mass range. Our results are consistent with those of JS for haloes of low-mass clusters, but yield a steeper mass dependence of axial ratios than a simple extrapolation of the scaling relations found by JS. This difference is important in the interpretation of observations on galaxy scales (Allgood et al. 2005) and, as we show here (Section 3), in the interpretation of X-ray ellipticities of samples containing very massive clusters. Our results are in agreement with those of Kasun & Evrard (2004) if axial ratios are calculated in the same manner. However, we find here that axial ratios calculated that way are not useful for predictions of cluster observables such as X-ray or SZ maps (see Appendix A). A source of uncertainty in the current understanding of halo shapes is the magnitude of the effect of gas cooling on cluster DM haloes (Kazantzidis et al. 2004; Springel et al. 2004).

The variety of current and future observational probes of halo ellipticity (see Paper I for a discussion) highlights the need to connect these predictions to observations in a robust fashion. Here we present an analytic method for predicting gravitational potentials and cluster gas density based on axial ratios of dark matter haloes. We test the model against a sample of 8 high-resolution hydrodynamic ART simulations of 7 clusters (mass $(1 - 2) \times 10^{14} h^{-1} M_\odot$) and 1 group (mass $7 \times 10^{13} h^{-1} M_\odot$) in the Λ CDM cosmology

(Kazantzidis et al. 2004), whose highly variant morphology dependence on the line of sight we exploit to statistically test the model, and 2 additional clusters from earlier high-resolution simulations (Kravtsov, Klypin, & Hoffman 2002; Nagai & Kravtsov 2003). We then apply the model to the prediction of ellipticities for cluster X-ray and SZ maps. A perturbative model has been developed by Lee & Suto (2003), and further extended by Wang & Fan (2004) to predict observed distributions from halo shape distributions, but it is not useful for our purposes here because the ellipticities can be quite large.

In the following section we discuss the analytic model we use to predict cluster X-ray and SZ morphologies, and we test it by comparing predictions for morphology of the simulation clusters (based on their DM haloes only) with the same observable computed directly from the gas density grid of the hydrodynamic simulations. In Section 3 we focus on observations and compare our predictions to several observational samples of cluster X-ray ellipticities. We also discuss recent papers (e.g. Floor et al. 2003; Floor, Melott, & Motl 2004) that have compared observed cluster shapes measured using X-rays and galaxy distributions to hydrodynamic simulations. We finish with a summary of our conclusions. The details of the comparison techniques used in Section 3 are outlined in three Appendices: A. Gas Density Inside Triaxial Halos; B. Analytic Potential of Triaxial Generalized NFW Halos; and C. A Comparison of X-ray Ellipticity Measures.

2 COMPARISON OF MODEL AND SIMULATION STATISTICS

In this section we analyse the prediction for two statistics of cluster morphology, the mean and the dispersion of their ellipticity distribution, expected in a flat Λ CDM universe with $\Omega_m = 0.3$, $h = 0.7$, and $\sigma_8 = 0.9$. We first discuss the method to predict cluster ellipticities based on their dark matter haloes, and then present the comparison of the predictions to the results from the output of several high-resolution hydrodynamical simulations (Kazantzidis et al. 2004). In what follows, the virial radius is defined as the radius, r_{vir} , within which the mean overdensity drops to $\Delta = 18\pi^2 + 82(\Omega_m(z) - 1) - 39(\Omega_m(z) - 1)^2$ (Bryan & Norman 1998). Masses are defined as the mass within r_{vir} .

2.1 Method

We use a diagonalized moment of inertia tensor iteratively calculated within ellipsoids, or ellipsoidal shells, to define axial ratios for dark matter haloes (Dubinski & Carlberg 1991). Axial ratios $s = c/a$ and $q = b/a$ ($s < q < 1$) are calculated by diagonalizing the tensor

$$M_{ij} \equiv \Sigma \frac{x_i x_j}{R^2}; \quad R = \sqrt{x^2 + y^2/q^2 + z^2/s^2}, \quad (1)$$

thereby determining s and q for the next iteration. The sum is over all particles within a given shell $[R, R + \Delta R]$, or the ellipsoid interior to R , and the iteration starts with $s = q = 1$. In Paper I we have found that this method predicts axial ratios that agree with the results of JS, which are based on isodensity shells, for cluster-size haloes, provided that the axial ratios be calculated within an ellipsoid of semi-major

axis $R = 0.3r_{\text{vir}}$. Here we also find that the same axial ratios can be used to predict fairly accurately the mean and dispersion of the expected X-ray ellipticities, even though as often as half the time the predicted ellipticity of an individual cluster is off by more than 20%.

The X-ray surface brightness of an isothermal cluster is given by an integral over the gas density squared along the line-of-sight (LOS) of a cluster, $\text{SB} \propto \int \rho_{\text{gas}}^2 \sqrt{T} \propto \int \rho_{\text{gas}}^2$. As discussed in Appendix A, under the assumptions of hydrostatic equilibrium and isothermality, the gas density at any point inside a triaxial homeoidal halo can be written in terms of the temperature T , the central gas density, and the halo potential at the desired point (Eq. A1). If we assume that the halo potential is dominated by the dark matter, then the relation is simplified by the fact that the potential of any triaxial generalized NFW halo is analytic (Appendix B). Thus, using the relation (A1), we can estimate the X-ray ellipticities implied by a dark matter halo given the halo axial ratios, and an orientation of a LOS corresponding to each of the simulation-box axes.

The only (slight) ambiguity in relating the gas density to the halo potential is the factor Γ in equation A1, which relates the gas density to the potential exponentially: $\rho_{\text{gas}} \propto \exp(-\Gamma\Phi)$. In Appendix C, we find that the analytic model works relatively well with $\Gamma \sim c_{\text{vir}}$ when we compare to two high-resolution clusters. This is roughly expected for an NFW halo since

$$\Gamma \simeq sq\rho_s R_s^2 \frac{G\mu m_p}{kT} \simeq \frac{\sigma^{-2} GM_{\text{vir}}}{r_{\text{vir}} f(c_{\text{vir}})} c_{\text{vir}} \sim c_{\text{vir}}, \quad (2)$$

where $f(x) = \ln(1+x) - x/(1+x)$ and σ is the LOS velocity dispersion. In the second step we have used $sq\rho_s R_s^2 \simeq \rho_{\text{sph}}^2 r_s^2$, where ρ_{sph} and r_s are spherical-NFW-fit parameters for the halo, and assumed the expected energy scaling, $kT \simeq \mu m_p \sigma^2$, which is even seen observationally (see e.g. Rosati, Borgani, & Norman 2002 and references therein), albeit with a fair amount of scatter. The final step follows from rough scaling relations, and works in detail for the clusters we consider in Appendix C.¹ Therefore, for our comparisons we assume

$$\frac{GM_{\text{vir}}\mu m_p}{r_{\text{vir}} f(c_{\text{vir}})kT} = 1, \quad (3)$$

and use $\Gamma = c_{\text{vir}}$. For the dark matter halo of the SCDM (Λ CDM) cluster, we find a value of 1.06 (0.98) for the RHS of this equation, using the average temperature of the gas inside a radius of $400 h^{-1}$ kpc.

2.2 Results

For a given dark matter halo, the method discussed above allows us to compute the SB map expected for a given LOS

¹ For example, for the SCDM (Λ CDM) cluster discussed there, $GM_{\text{vir}}/r_{\text{vir}} f(c_{\text{vir}}) = 1063$ (630) km/s. The dispersion inside the relevant projected radius ($400 h^{-1}$ kpc) for these clusters is similar to these values. For the SCDM cluster, the dispersion is $\sigma = 1116$ km/s (1077 km/s, 1000 km/s) along the x-axis (y-axis, z-axis). For the Λ CDM cluster, we find $\sigma = 661$ km/s (928 km/s, 650 km/s). The higher σ along the y-axis is due to a merger nearly along this axis; however, the same Γ chosen to fit the radial fall-off in surface brightness in the plane perpendicular to the x-axis works well for the other two axes.

through that halo. We discuss in Appendix C how an X-ray ellipticity can be obtained from the SB map. There is no unique method to calculate ellipticities and, as we discuss below and in Appendix C, it is important to follow the procedure chosen by observers to calculate ellipticities in order to compare to observations. *Individual* ellipticities can differ *substantially* depending on what part of a map the procedure selects and, as we show below, *even the means* (of samples of ellipticities calculated with different procedures) *will differ*.

Figure 1 shows SB maps for 8 high-resolution *adiabatic* hydrodynamic simulations of clusters in the Λ CDM cosmology (see Kazantzidis et al. 2004). Each row in the figure shows the 3 SB maps corresponding to a LOS parallel to each of the coordinate axes of the simulation box containing the cluster. We calculate the SB for a given ‘‘pixel’’ in each box by summing $\rho_{\text{gas}}^2 \sqrt{T}$ over all cells along the LOS-axis. Each cell is $7.8 h^{-1}$ kpc on the side, and each map covers $2 h^{-1}$ Mpc on the side. The X-ray ellipticity, ϵ_X , shown in the upper right corner of each map, is calculated using the pixels (shown by the shaded areas) containing 20% of the total flux above a threshold flux that is 1% of the peak flux of the map. This is one of the procedures we consider in this work to calculate ellipticities from a SB map. It is a method that in the absence of noise yields ellipticities that reflect the potential of the DM halo, as we show in the next paragraph. McMillan et al. (1989) used this method in their study of X-ray ellipticities. However, we find below (see Section 3) that their data are heavily affected by noise and do not serve as a test of the Λ CDM cosmology. A more detailed discussion of methodologies is presented in Appendix C.

For each cluster halo we can use the method described in Section 2.1 to compute the predicted SB map for a given LOS through a given cluster. We can then compute the predicted X-ray ellipticity in exactly the same manner we computed the ellipticity for the hydrodynamic simulation maps of Figure 1. In Figure 2 we show a comparison of the two ellipticities. Each point in the figure plots the ellipticity shown in Figure 1 against the ellipticity calculated based only on the DM halo parameters. A Kolmogorov–Smirnov (KS) test gives high probability ($P_{KS} = 99\%$) that the two sets represent the same distribution. We treat the value of ϵ_X for each LOS as an independent measurement because for a given axial ratio s there is quite a degree of variability expected for the other axial ratio, and then there is the variation introduced by the orientation of the cluster to the LOS. There is indeed quite a degree of variation in ϵ_X for each cluster, but a stronger test will only be possible with many more simulations. The means of the sets indeed agree quite well: $\langle \epsilon_X^{\text{hydro}} \rangle = 0.36$, whereas $\langle \epsilon_X^{\text{model}} \rangle = 0.35$. However, the dispersions differ significantly: $\sigma_{\epsilon}^{\text{hydro}} = 0.18$, whereas $\sigma_{\epsilon}^{\text{model}} = 0.12$. This is due to the middle map in the last row of Figure 1, whose ellipticity is greatly enhanced by a secondary lump that in this case has a significant relative weight due to fact that the flux levels select a narrow region of the main cluster. Without that map, $\langle \epsilon_X^{\text{hydro}} \rangle = 0.34$, and $\sigma_{\epsilon}^{\text{hydro}} = 0.15$ (recalculating the ellipticity without the lump, $\langle \epsilon_X^{\text{hydro}} \rangle = 0.35$ and $\sigma_{\epsilon}^{\text{hydro}} = 0.15$). The remaining difference between $\sigma_{\epsilon}^{\text{hydro}} = 0.15$ and $\sigma_{\epsilon}^{\text{model}} = 0.12$ seems to be due to the fact that the gas reflects the changing triaxiality in the inner region of DM haloes. We tested this by recalculating $\epsilon_X^{\text{model}}$ using axial ratios for the DM

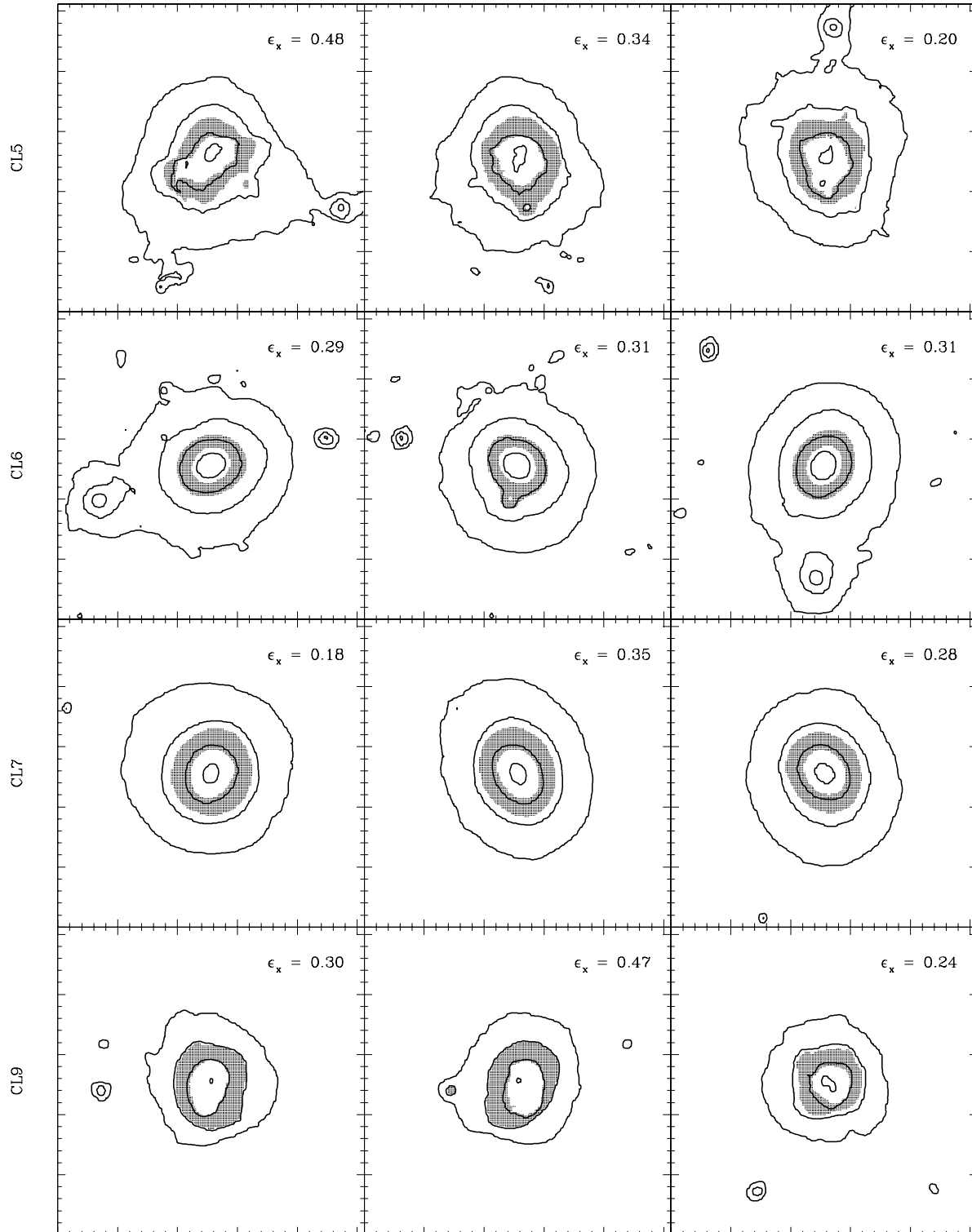


Figure 1. X-ray SB maps for hydrodynamic simulation clusters. Each row presents the SB for a LOS along each of the axes of the simulation box. Each square is $2 h^{-1}$ Mpc across. The solid lines show contours of constant SB, spaced by factors of 10. The shaded area is the region used to calculate the ellipticity shown in the upper right corners. See text for explanation and discussion.

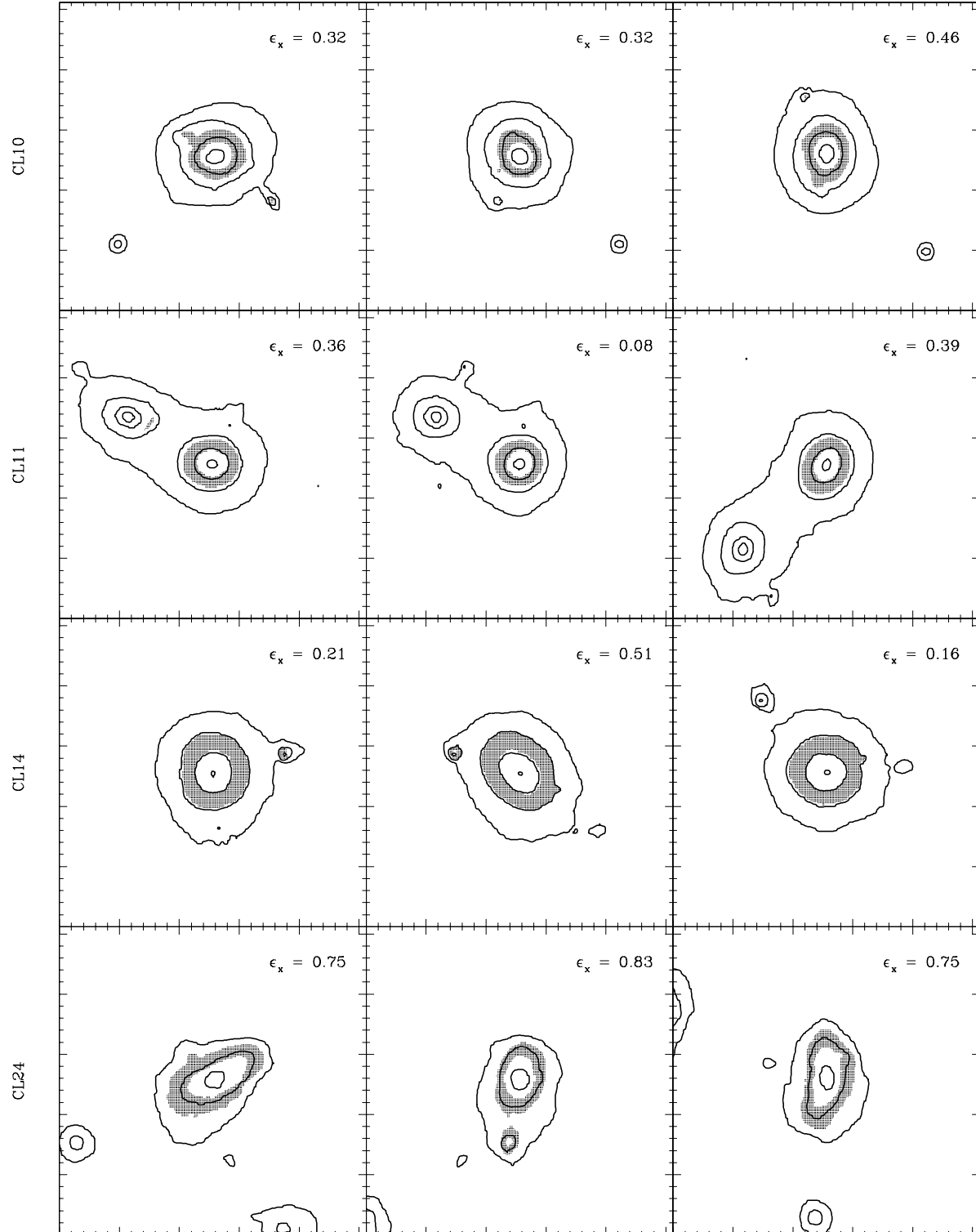


Figure 1. Continued

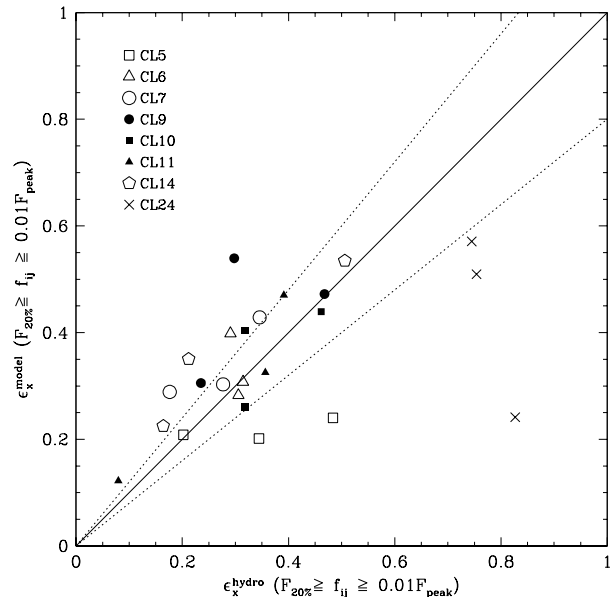


Figure 2. Model X-ray ellipticities compared to the ellipticities calculated directly from SB maps for the hydrodynamic simulation clusters. Each symbol identifies a cluster, and for each cluster the symbol plots the ellipticity calculated from the simulation map (one for each LOS along each of the coordinate axes) against the predicted ellipticity using the method described in Section 2.1. Within the dotted lines the ellipticities differ by less than 20%.

haloes calculated within $R = 0.15r_{\text{vir}}$, in which case we find $\langle \epsilon_X^{\text{model}} \rangle = 0.35$ and $\sigma_{\epsilon^{\text{model}}} = 0.15$.

Thus, the analytic model can be used to make fairly robust predictions of average X-ray ellipticities. An equally robust prediction of the expected scatter does not seem possible with a simple homeoidal model of DM haloes, but its reliability might be checked by calculating two sets of ellipticities based on DM halo axial ratios calculated within two different radii. We have used the model, then, to calculate the mean and dispersion of X-ray ellipticities expected in a Λ CDM universe at the present epoch. We use a sample of 46 DM haloes extracted from the $120 h^{-1}$ Mpc dissipationless cosmological simulation discussed in Paper I. The cosmology is a flat Λ CDM universe with $\Omega_m = 0.3$, $h = 0.7$, and $\sigma_8 = 0.9$ and the simulation followed 512^3 particles of mass $1.1 \times 10^9 h^{-1} M_\odot$. All haloes with virial mass $(1 - 4) \times 10^{14} h^{-1} M_\odot$ were selected. We calculate their axial ratios and concentrations in order to predict X-ray ellipticities for a LOS corresponding to each of the coordinate axes of the box. The ellipticity is computed as described above, using two flux levels. The samples corresponding to each LOS agree quite well with each other. For the combined sample we find

$$\langle \epsilon_X \rangle = 0.323 \pm 0.013; \quad \sigma_\epsilon = 0.138 \pm 0.008, \quad (4)$$

where the errors are calculated by bootstrap resampling. These results are consistent with those for the hydrodynamic simulation clusters, for which $\langle \epsilon_X \rangle = 0.338 \pm 0.032$ and $\sigma_\epsilon = 0.148 \pm 0.030$.

The strategy to extract an X-ray ellipticity from a SB map is by no means unique, and in Figure 3 & Figure 4 we present two other cases of interest here. For example, in Sec-

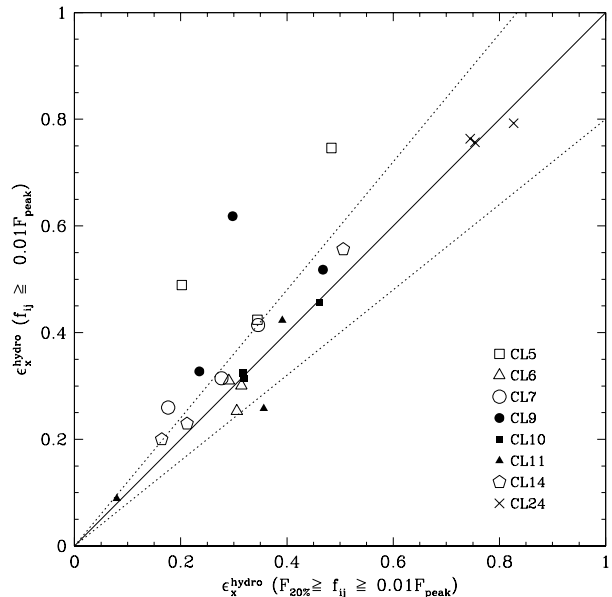


Figure 3. Comparison of ellipticities calculated directly from SB maps of the hydrodynamic simulation clusters using different strategies. The abscissa is the same as in Figure 2. The ordinate is an ellipticity calculated using *all* pixels above a given flux threshold, in this case 1% of the peak flux in a map. Within the dotted lines the ellipticities differ by less than 20%. See text for further discussion.

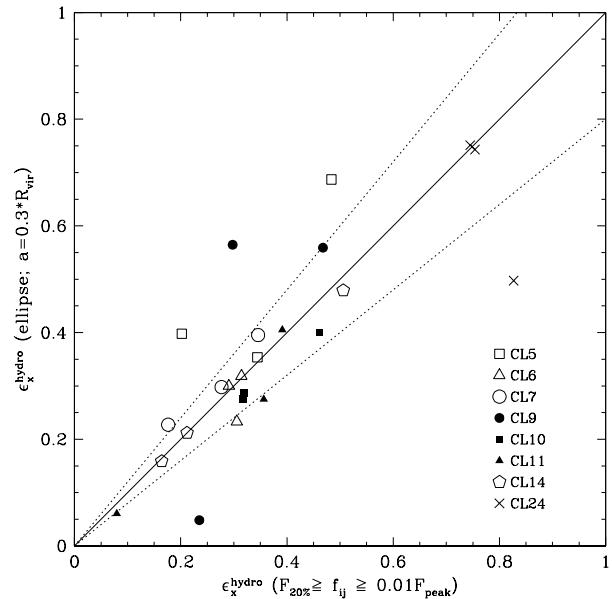


Figure 4. Comparison of ellipticities calculated directly from SB maps of the hydrodynamic simulation clusters using different strategies. The abscissa is the same as in Figure 2. The ordinate is an ellipticity calculated iteratively using *all* pixels within an elliptical aperture of fixed semi-major axis $a = 0.3r_{\text{vir}}$. Within the dotted lines the ellipticities differ by less than 20%. See text for further discussion.

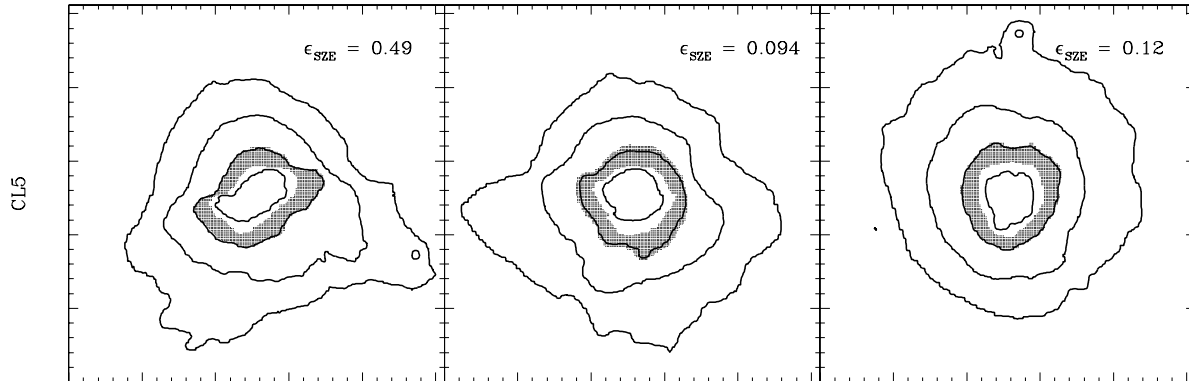


Figure 5. Sunyaev–Zel’dovich decrement maps for a hydrodynamic simulation cluster. Each panel presents the map for a LOS along each of the axes of the simulation box. Each square is $2 h^{-1}$ Mpc across. The solid lines show contours of constant temperature decrement, spaced by factors of 3. The shaded area is the region used to calculate the ellipticity shown in the upper right corners. See text for explanation and discussion.

tion 3 we discuss a sample of X-ray ellipticities obtained by Kolokotronis et al. (2001) who use a strategy that emphasizes the central region of a cluster (they were interested in mergers). In Figure 3 we show a comparison of ellipticities (all calculated directly from the hydrodynamic simulation maps) using two different strategies. The ordinate is an ellipticity very similar to that of Kolokotronis et al. (2001), calculated using all pixels above a flux threshold corresponding to 1% of the peak flux of the SB map. The abscissa is as in Figure 2. It can be seen there that they differ systematically from one another: the means differ by 14%. Therefore, a direct comparison of a sample of ellipticities calculated in this fashion to our predictions, (Eq. 4), is not possible.

Another example of interest here is the strategy used by Buote, Hart, & Humphrey (2005). They calculate ellipticities using *all* pixels inside a smooth boundary (i.e. the boundary is not determined by flux level), which is determined by applying the method of Carter & Metcalfe (1980) (used without iteration in the studies of McMillan et al. 1989 and Kolokotronis et al. 2001 as explained in Appendix C) iteratively, starting from a circle, until the ellipticity converges with a given accuracy. The semi-major axis is kept fixed. Figure 4 shows a comparison of ellipticities (all calculated directly from the hydrodynamic simulation maps), calculated using the methodology of Buote et al. (2005) (ordinate) and McMillan et al. (1989) (abscissa). The ellipticities agree quite well in mean value and dispersion ($P_{KS} = 89\%$), despite the fact that the methodology of Buote et al. (2005) uses all pixels within the elliptical window. Thus, the choice of a smooth boundary (rather than a flux-selected boundary) makes the ellipticity samples differ in no systematic way, unlike the case of Figure 3. A comparison of a sample of ellipticities calculated this way to our predictions, (Eq. 4), is therefore possible.

Finally, we also explore here the reliability of the analytic model to predict the expected ellipticity of millimeter-wave maps of the SZ effect (SZE) in clusters (see e.g. Carlstrom et al. 2002), which map the effective temperature decrement of the microwave background due to the hot elec-

tron gas (Sunyaev & Zel’dovich 1970). Figure 5 shows decrement maps for one of the clusters in Figure 1 (CL5), with contours spaced by a factor of 3 (the maps for all clusters are included as supplementary material). The maps are qualitatively similar to the SB maps, but the effect of changing triaxiality of the DM haloes in the region spanned by the isodecrement contours shown is more readily noticed (because the signal is proportional ρ_{gas} instead of ρ_{gas}^2). We show in the upper right corner of each map the ellipticity obtained in the same manner as Figure 1, but the decrement threshold and the percentage of signal in the pixels are chosen so that the pixels used cover a region of similar size to the corresponding region in Figure 1. Specifically, the decrement threshold chosen is 10% of the peak decrement in the map (as opposed to the 1% of peak signal in Figure 1), and the signal in all of the pixels used is 30% of the total signal above the threshold (as opposed to the 20% in Figure 1). The mean ellipticity and the scatter for this set are $\langle \epsilon_{SZE} \rangle = 0.307 \pm 0.035$ and $\sigma_{SZE} = 0.171 \pm 0.019$, respectively (bootstrap resampling errors). For the set of Figure 1, but with 10% threshold and 30% flux, $\langle \epsilon_X \rangle = 0.359 \pm 0.036$ and $\sigma_X = 0.175 \pm 0.033$, respectively (the difference with our 1% threshold and 20% flux prediction above is due to the changing triaxiality of DM halos). By contrast, the analytic model would predict nearly identical distributions. Thus, although not as successful as for X-ray ellipticities, the analytic model would still be useful to predict, e.g. quantitative trends for ellipticities as a function of cluster redshift.

We now turn to a quantitative comparison of the expected distribution of X-ray ellipticities in the Λ CDM cosmology, obtained using the analytic model we have discussed and tested here, with observational samples.

3 COMPARISON TO CLUSTER-SCALE OBSERVATIONS

Here we compare our predictions to ellipticity distributions from samples of cluster X-ray observations. We first anal-

use the methodology employed by McMillan et al. (1989) and Kolokotronis et al. (2001) to calculate ellipticities for their samples of Abell clusters. We also consider briefly the sample of Mohr et al. (1995) considered by Wang & Fan (2004) for their comparison to observations. These samples use different methodology to calculate ellipticities, and are affected differently by resolution and noise. Applying a KS test to pairs of samples (all converted to 2D axial ratios) we find that $P_{KS} = 0.0031$ ($P_{KS} = 0.21$) for the McMillan et al. (1989) and Mohr et al. (1995) samples (Kolokotronis et al. (2001) and Mohr et al. (1995) samples). This complicates the comparison of theoretical predictions and observations, but it is usually ignored (e.g. Melott et al. 2001; Wang & Fan 2004). Finally, we analyse a very recent data set from a nearly complete, flux-limited sample of *ROSAT* clusters discussed by Buote et al. (2005).

Mohr et al. (1995) considered a sample of 51 (mostly Abell) clusters observed by the *Einstein* IPC, for which they obtained a mean 2D axial ratio, η , of $\langle\eta\rangle = 0.80$ and a dispersion $\sigma_\eta = 0.12$. Converting their axial ratios to ellipticities, $\epsilon = 1 - \eta^2$, we obtain $\langle\epsilon\rangle = 0.358 \pm 0.026$ and $\sigma_\epsilon = 0.182 \pm 0.017$. The mean and scatter differ by about 1.5 and 2.5 standard deviations, respectively, from our predictions (Eq. 4). However, the method of Mohr et al. (1995) uses all pixels above a S/N level, and therefore gives substantially more weight to the central regions of a SB map, where mergers can significantly affect the ellipticity. Given our discussion of the results presented in Figure 3, the difference in mean ellipticity (10%) is entirely within the expectation given the different strategy. The agreement is somewhat surprising, however, given the potential effect that cooling within clusters could have on the DM haloes (Kazantzidis et al. 2004; Springel et al. 2004). We discuss this further below.

The Kolokotronis et al. (2001) sample consists of 22 *ROSAT* clusters, with a range of velocity dispersions of 400 – 1000 km/s. Converting their ellipticities to $\epsilon = 1 - \eta^2$, the mean and dispersion of their sample are $\langle\epsilon\rangle = 0.458 \pm 0.051$ and $\sigma_\epsilon = 0.237 \pm 0.023$. The poor agreement with our prediction (Eq. 4) is not surprising given that their method emphasizes the cluster centre and there are three clusters in the observational sample showing strong evidence of an ongoing merger: A2804, A2933, and A3128 are all bimodal (Kolokotronis et al. 2001). We have tested that this is indeed the problem by computing ellipticities for the sample of hydro clusters discussed in Section 2, following exactly the procedure of Kolokotronis et al. (2001), which first defines a flux threshold equal to the mean flux within a $600 h^{-1}$ kpc radius, and then uses all pixels above the threshold. A KS test between the hydro sample of ellipticities calculated this way, and the sample of Kolokotronis et al. (2001), gives $P_{KS} = 0.82$ (the hydro sample is slightly rounder on average). Thus we conclude that their sample is in agreement with the expectations for a Λ CDM universe.

We have also made a comparison with the *Einstein* data of McMillan et al. (1989) consisting of 49 clusters. Here we can expect the comparison to be a better test on the cosmological sample because they explicitly exclude image centres, thus their shape statistic is less sensitive to mergers (see Appendix C). However, the mean and dispersion of their sample are $\langle\epsilon\rangle = 0.240 \pm 0.020$ and $\sigma_\epsilon = 0.142 \pm 0.015$. There is poor agreement with our prediction (Eq. 4) for the mean

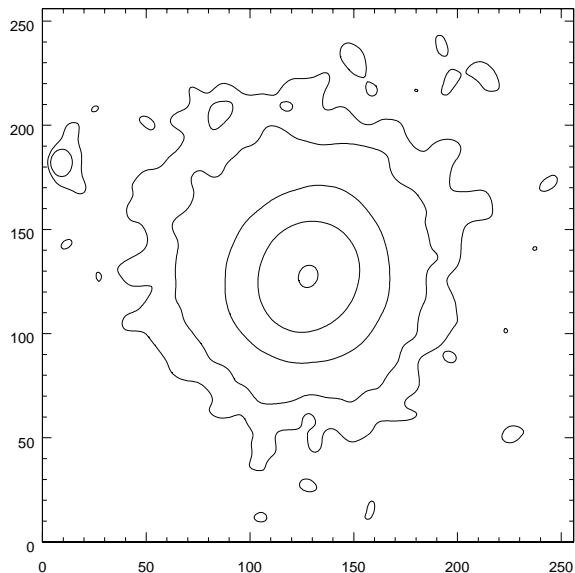


Figure 6. Simulated X-ray map of a hydrodynamic simulation cluster (CL7) after smoothing and adding noise. See text for discussion.

this time. It appears unlikely that this discrepancy could be entirely due to missing physics (e.g. cooling) in the simulations we have used to test the analytic model described in Appendix A. We note that even after excluding the 3 bimodal clusters from the Kolokotronis et al. (2001) sample, a KS test against the McMillan et al. (1989) sample (once ellipticities are converted to the same definition in terms of flux-moment eigenvalues; see Appendix C) rejects that they are compatible at the 96% CL.

The coarser angular resolution of the *Einstein* data probably contributes to this disagreement. For example, we find that if we smooth the X-ray map of the Λ CDM cluster we discuss in Appendix C (see Figure C1) with a gaussian window of $80 h^{-1}$ kpc (FWHM, roughly corresponding to the $1.6'$ resolution of the McMillan et al. (1989) data at the median redshift of their sample, $z = 0.057$), the X-ray ellipticities can change significantly: the entry in column 6 of Table C1 would be 0.40 (0.23, 0.46) for the x-axis (y-axis, z-axis) as compared to 0.43 (0.28, 0.51) without smoothing. This is also consistent with the changes found by Buote & Canizares (1996) for 5 clusters with *Einstein*, later analysed with *ROSAT* data. We find that a 20% change in the predicted ellipticities would make them marginally compatible with the data.

A more important contribution to the difference with our predictions seems to be the effect of noise. Many clusters in the McMillan et al. (1989) sample have very small ellipticities but do not look round at all. Figure 6 shows the effect of smoothing and noise on one of the clusters in Figure 1 (CL7, left). The noise level is at 70% of the threshold (1% of peak flux) used for the calculation of ϵ_X . The automated software of McMillan et al. (1989) allowed up to 50 islands in the X-ray map, thus this map would be accepted. The ellipticity without smoothing and noise would be $\epsilon_X = 0.18$ in this case, but with smoothing and noise (the latter mak-

ing the largest difference) $\epsilon_X = 0.08$. If we put this level of noise in all the hydro clusters, we find that the hydro sample becomes fully compatible with the McMillan et al. (1989) sample: $P_{KS} = 0.87$. Thus, it may be that our predictions are not incompatible with this data sample.

Finally, we discuss the recent sample of ellipticities obtained by Buote et al. (2005) for the flux-limited sample of *ROSAT* clusters of Reiprich & Böhringer (2002). As we showed in Section 2.2, a direct comparison to our predictions (Eq. 4) is in this case possible. It is worth emphasizing here that an important advantage of these data is that all the ellipticities are calculated within the *same* aperture ($0.3r_{\text{vir}}$). The mean and dispersion for the sample of Buote et al. (2005) are $\langle \epsilon_X \rangle = 0.376 \pm 0.019$ and $\sigma_\epsilon = 0.122 \pm 0.014$, respectively ($\epsilon = 1 - \eta^2$). The dispersion is less than expected, but only by approximately 1σ . However, the mean is substantially larger than expected (by approximately 2.8σ). This appears to be due to the expected mass dependence of axial ratios.

As discussed in Paper I, dark matter haloes are systematically more triaxial the larger their mass. A simple relation was found that describes this behavior: $\langle s \rangle = 0.54(M_*/M_{\text{vir}})^{0.05}$ (see Paper I). Many of the clusters in the sample discussed by Buote et al. (2005) are much more massive than the sample of simulation clusters we used to make our predictions (Eq. 4). This is to be expected because the observational sample was flux limited and, therefore, massive clusters are overrepresented (relative to a volume-limited sample, which the simulation clusters represent). Using the scaling relation above, we find that our prediction for the mean ellipticity of a sample of clusters with a mass function like that of the clusters analysed by Buote et al. (2005) would be $\langle \epsilon_X \rangle = 0.353 \pm 0.013$ (instead of Eq. 4).² The remaining difference could well be a statistical fluctuation, given that the intrinsic dispersion in ellipticities is $\sigma_\epsilon \sim 0.14$. Thus, we can expect fluctuations $O(\sigma_\epsilon/\sqrt{N}) = 0.022$ for a sample of the size of the Buote et al. (2005) sample. By contrast, if we assume the milder scaling advocated by JS, $\langle s \rangle = 0.54(M_*/M_{\text{vir}})^{0.03}$, the predicted mean ellipticity would be $\langle \epsilon_X \rangle = 0.312 \pm 0.011$ instead, which is 3.4σ lower than the observations. It is also worth pointing out that the data themselves show evidence of mass dependence, although not at a high level of confidence. If we split the data of Buote et al. (2005) by mass, for clusters below (above) $M_{\text{vir}} = 10^{15} h^{-1} M_\odot$ $\langle \epsilon_X \rangle = 0.357 \pm 0.027$ and $\sigma_\epsilon = 0.117 \pm 0.020$ ($\langle \epsilon_X \rangle = 0.393 \pm 0.026$ and $\sigma_\epsilon = 0.123 \pm 0.019$). There are about equal number of clusters in each subsample. Although the difference in mean value is not highly significant, it is of the magnitude expected (10%) using the scaling of Paper I.

We conclude from the comparison with these four data samples that the predictions for cluster X-ray shapes in the Λ CDM cosmology, *assuming gas cooling has only a small effect on the shape of their dark matter haloes*, are in good agreement with the data. A more stringent test, however,

would require a larger sample of clusters and a better quantitative understanding of the effect of cooling.

We have attempted to estimate quantitatively the effect of gas cooling on cluster X-ray ellipticities, which generically makes DM haloes less triaxial. We use a hydrodynamic simulation of one cluster for which cooling and star formation was abruptly terminated at redshift $z = 2$ in order for the cluster to have reasonable star and gas fractions (see Kazantzidis et al. 2004). The effect of cooling on DM halo axial ratios for this cluster agrees very well with the *average* effect shown in Figure 4 of Springel et al. (2004). We calculated the short/long axial ratio in logarithmic radial distance bins in order to directly compare to the figure in Springel et al. (2004). We find that there is good agreement in the distance range $(0.1 - 0.3)r_{\text{vir}}$. Therefore, we have estimated the expected effect on X-ray ellipticities in two ways. We can compute the change in ellipticity by comparing the ellipticities with and without cooling for this one cluster. Since the change in axial ratios seems to be representative of the expected average change, we can estimate that the effect would be to make X-ray ellipticities 10–20% smaller. We have also estimated the effect by generating a catalog of DM “haloes”, where a halo is represented as a set of axial ratios and a concentration. We generate axial ratios using the form of the distribution of s and q found in simulations (we use $\bar{s} = 0.54$ and $\sigma_s = 0.1$ for the gaussian distribution of s ; Paper I). We generate concentrations using the lognormal distribution of Wechsler et al. (2002), with mean of 7 and a log-dispersion of 0.14. Finally, we orient randomly the principal axes in a box. A mean short/long axial ratio $\bar{s} = 0.54$ instead of $\bar{s} = 0.45$ adequately represents the effect seen on average by Springel et al. (2004), and the effect on the cluster discussed here. We find in this case that we can expect X-ray ellipticities to be $\sim 25\%$ smaller. It is thus rather surprising that we find the level of agreement with the data that we have found here *without* taking the effect of cooling into account.

We have considered a lower- σ_8 cosmology, in which DM halos are predicted to be more triaxial (see Paper I), as a possible explanation of this surprising result. If DM halos were more triaxial, the predicted X-ray ellipticities would increase and then cooling could bring results into agreement with the data. We have found in Paper I that a simple scaling relation accounts for the dependence of axial ratios on σ_8 (see Paper I, Eq.(7)). The predicted \bar{s} can then be used as above to generate a catalog of axial ratios. We find that even for a value of σ_8 as low as $\sigma_8 = 0.75$, the expected mean X-ray ellipticity of a sample like the Buote et al. (2005) sample changes only to $\langle \epsilon_X \rangle = 0.378 \pm 0.013$ (from $\langle \epsilon_X \rangle = 0.353 \pm 0.013$ for $\sigma_8 = 0.9$).

There are potential biases that can affect comparisons of the model with observations. For example, in relaxed cooling flow clusters the temperature decreases toward the center in the cluster core (e.g., De Grandi & Molendi 2002; Vikhlinin et al. 2005a). Line emission of low-temperature X-ray gas can significantly alter the $\rho_{\text{gas}}^2 \sqrt{T}$ weighting assumed in our analysis and, therefore, the shape of the X-ray brightness isophotes. To take this effect into account, however, we need to know the temperature and metallicity distribution in clusters. We plan to address this issue in future work, which will make use of the cluster simulations with galaxy formation. However, Buote et al. (2005) have calculated el-

² We do the calculation by generating a Monte Carlo set, picking the observationally estimated mass of a cluster, and using the scaling relation above to get a corresponding $\langle s \rangle$. We then draw axial ratios for the cluster using the form of the distribution of s and q found in simulations (see Paper I).

lipticities in annuli as well, i.e. excluding the cluster centers altogether. The mean ellipticity is only slightly (4%) higher.

Another possible source of bias can arise in comparisons with the shape estimates based on the isophotes defined at a constant fraction of the peak flux of the cluster. The profiles of real clusters are often quite “cuspy” in their centers (e.g., Vikhlinin et al. 2005b) and are considerably steeper than the radial gas density profiles of clusters in our adiabatic simulations. This difference in the radial gas distribution will result in different radii of the isophotes defined with respect to the peak flux. This may mean that the shapes would be measured at systematically different radii in simulations and observations (smaller radius in observations). Note, however, that Buote et al. (2005) calculate ellipticities within the same aperture, as we have stressed above.

Two qualitative trends in X-ray maps appear to reflect the more complex nature of dark matter haloes seen in high resolution simulations. Buote & Canizares (1996, and references therein) have pioneered detailed studies of X-ray maps to constrain cluster halo profiles. They studied 5 Abell clusters using oblate and prolate spheroids in order to bracket the possibilities, and concluded that the ellipticity (there is only one axial ratio if one assumes oblate and prolate spheroids) of the haloes was constrained to be in the range 0.40 – 0.55. The systematic trend of interest here is that 4 of the 5 clusters show a decreasing ellipticity of the X-ray isophotes at larger radii. A similar trend can be seen in the gas data for the two high-resolution simulation clusters discussed in Appendix C (see Figure C1 and Figure C2) and is due to the decreasing triaxiality of the dark matter halo at larger radius. The effect is not very pronounced, so the simple isothermal/homeoidal halo model could still be used for the ellipticity comparison above. The same is not true, however for Sunyaev–Zel’dovich decrement maps (see Figure C3). As discussed in Appendix C, the different sensitivity of SZ maps to density and temperature ($\propto \int \rho_{gas} T$) make these observations more sensitive to our simplistic assumptions, and the simple mapping from halo shape parameters will break down more visibly. More detailed modeling will likely be required to interpret SZ shape measurements accurately.

A second complication of interest here was noted by McMillan et al. (1989), who pointed out that a fraction ($\sim 15\%$) of their clusters exhibited isophotal twist with a “continuous rotation of the intermediate isophotes”. We have found that one of the high-resolution simulation clusters discussed in Appendix C (see Figure C2) shows this kind of twist due to coherent twist of the dark matter density shells. Of course, it will be interesting to quantify the frequency of this effect, as well as its origins. The degree of misalignment in the case of this cluster ($\sim 45^\circ$ in the radial range $\sim (0.3 - 1)r_{vir}$) would be rare judging by the results of JS for 12 haloes. However, a direct comparison is not possible because the angles involved are not the same.

Therefore, while some observational quantities are somewhat insensitive to the complex non-homeoidal nature of halo structure, many observed properties are quite sensitive to changing ellipticities and twists. Specifically, the higher-order trends in halo shapes may leave imprints in cluster gas that could be studied in detail by analyses of X-ray and Sunyaev–Zel’dovich maps.

Clusters X-ray ellipticities can be expected to evolve

with redshift due to increased halo triaxiality (see Paper I, and references therein). Recent papers have called attention to a possible significant evolution of the ellipticity with redshift even over the nearby redshift range $z = 0 - 0.1$ (Melott, Chambers, & Miller 2001; Plionis 2002), and have claimed that cluster X-ray and optical profiles are a little less flattened than predicted by dissipationless and hydrodynamic simulations (see Floor et al. 2003; Floor et al. 2004; and references therein). However, it is important to compare observational data to simulated clusters of similar mass (the Floor et al. clusters were more massive than most of the observed clusters) and, as we have explained (see Appendix C), to mimic the way the data was treated. It is hard to draw clear conclusions when the rather different McMillan et al. (1989) and Kolokotronis et al. (2001) X-ray data sets and analyses are combined, as was done by Melott et al. (2001). Jeltema et al. (2005) have detected evolution in cluster morphology in a more homogeneous sample of clusters with *Chandra* data. However, the morphology is not quantified as an ellipticity, therefore we cannot assess how well this observation constrains theory in our current paper.

4 CONCLUSIONS

We have presented a simple analytic model to predict cluster halo gas profiles based on dark halo shapes, under the assumption that clusters are isothermal and in hydrostatic equilibrium within haloes that are homeoidal ellipsoids (i.e. with constant axial ratios). We found that certain observational properties, such as ellipticities of X-ray surface brightness maps, can be adequately described by this modeling. When applied to our sample of cluster-mass haloes we find that the predicted distribution is in good agreement with observational samples of ellipticities for galaxy clusters. The agreement with the recent Buote et al. (2005) analysis of a complete *ROSAT* sample is especially impressive, because we found it important to take into account the predicted mass dependence of halo shape in comparing to this data sample rich in very massive clusters. The usefulness of our model is sensitive to how the observed ellipticity is defined. Specifically, care must be taken to avoid definitions that make the calculated ellipticities sensitive to mergers.

The shape of dark matter haloes undoubtedly cannot be fully characterized by simple models with constant axis ratios. While we have used inertia-tensor derived axial ratios to characterize halo shapes in a simple way, and explored how simple assumptions about halo shapes can be used to compare to observational tracers of halo structure, we find that more detailed predictions will be required for many observational comparisons (Appendix C). For example, the isothermal/homeoidal assumption becomes less useful for comparison to measurements like Sunyaev–Zel’dovich decrement maps. In addition, radially decreasing ellipticities can arise from the changing shape of isodensity contours with radius, and twists in X-ray isophotes can arise from misalignment of contours at large and small radius. Predictions aimed at this kind of data will require a more detailed analysis of Λ CDM halo shapes, including a detailed characterization of halo ellipticities as a function of radius, and the frequency of isophotal twists. Work in this direction is under way.

ACKNOWLEDGMENTS

We thank Daisuke Nagai and Andrew Zentner for their help. JSB was supported by NSF grant AST-0507816 and by startup funds at UC Irvine. AVK was supported by the NSF under grants AST-0206216 and AST-0239759, and by NASA through grant NAG5-13274. BA and JRP were supported by AST-0205944 and NAG5-12326. The numerical simulations used in this study were performed at the National Center for Supercomputing Applications (NCSA, Urbana-Champaign). This research has made use of NASA’s Astrophysics Data System Bibliographic Services.

APPENDIX A: GAS DENSITY INSIDE TRIAXIAL HALOS

Here we present a simple model of the gas density expected inside a cluster halo, and use it to calculate X-ray properties such as surface brightness. The model can also be used for other gas–density–dependent observations, such as SZE maps from millimeter–wave observations of clusters (see e.g. Carlstrom et al. 2002). We define the dark matter halo density model, and calculate its potential, in Appendix B. The gas density model is based on three common approximations about the gas:

- 1) the gas is in hydrostatic equilibrium,
 - 2) the gas is isothermal,
 - 3) the gas makes a negligible contribution to the total mass.
- These assumptions are quite restrictive, although it is trivial to modify equation (A1) below for a polytropic gas. In Appendix C we shall relax all of the assumptions and work directly with the gas in two high–resolution simulations of galaxy clusters. We work out expected X-ray properties for the clusters in the simulations, and compare them to the predictions based on the model described here. We find that the model works fairly well, despite its simplifying assumptions. We further test the model statistically against a small sample of high–resolution simulation clusters in Section 2.

With the assumptions listed above, the gas density expected at a point (x, y, z) inside a triaxial halo can be written in terms of the gas density at the origin, the dark matter potential $\Phi(x, y, z)$, and the gas temperature T . For the halo density model discussed in Appendix B, we find it convenient to work with the potential in units of the overall factor $4\pi Gsq\rho_s R_s^2$. Therefore, we write

$$\rho_{gas}(x, y, z) = \rho_{gas}(0) \exp \left\{ -\Gamma \left(\tilde{\Phi}(x, y, z) - \tilde{\Phi}(0) \right) \right\}. \quad (\text{A1})$$

Here $\tilde{\Phi}(x, y, z) = \Phi(x, y, z)/4\pi Gsq\rho_s R_s^2$, so the constant Γ is given by

$$\Gamma = 4\pi Gsq\rho_s R_s^2 \frac{\mu m_p}{kT}, \quad (\text{A2})$$

where μ is the mean molecular weight. For clusters with galaxy velocity dispersion σ , $kT \sim \mu m_p \sigma^2$ (see e.g. Rosati et al. 2002). Therefore, since $4\pi sq\rho_s R_s^2 = O(\sigma^2/G) c_{vir}$ (see Section 2), we can expect $\Gamma \sim c_{vir}$.

We can use this simple model to calculate the expected X-ray SB of hot gas in a dark halo with a given potential. Since we have assumed the gas is isothermal, SB

$\propto \int \rho_{gas}^2$, where the integral is calculated along the LOS. In Appendix B, we calculate the potential $\Phi(x, y, z)$ in the principal–axis coordinate system of the dark matter halo. Therefore, in order to calculate SB we need the orientation of the LOS in this coordinate system. We use the conventions of Binney (1985), in which the LOS–axis is defined by azimuthal and polar angles ϕ and θ , respectively.

We thus have the following model to predict the X-ray SB map expected for a given projection of a dark matter halo in a simulation box. We first calculate the axial ratios $s < q < 1$ by the iterative procedure described in Section 2; in Appendix C we find that axial ratios calculated using a solid ellipsoid of semi–major axis $0.5r_{vir}$ works well to predict flux–weighted ellipticities. We also obtain from the procedure the orientation (ϕ and θ) of a given LOS, and the orientation (position angle, PA) of the projection of the shortest axis of the halo on the plane perpendicular to the LOS. For a given point along the LOS, we find ρ_{gas} by first rotating its coordinates in the plane by the PA. We then apply the inverse of the rotation parametrized by ϕ and θ (Binney 1985). This gives us the coordinates of the point along the LOS in the principal–axis system, from which we obtain ρ_{gas} using equation (A1). Therefore, we can calculate $\int \rho_{gas}^2$ numerically at any given point on the plane. (We shall refer to this model for the SB as the “analytic model” even though it involves numerical integration), in order to distinguish its predictions from those we work out directly from the gas density in two high–resolution simulations of galaxy clusters that we analyse in Appendix C, where we compare predictions for X-ray ellipticities.

APPENDIX B: ANALYTIC POTENTIAL OF TRIAXIAL GENERALIZED NFW HALOS

Here we consider the potential of triaxial dark matter haloes with a density profile that is a simple generalization of a special case of the spherical profile introduced by Hernquist (1990). We assume that isodensity shells are homeoidal ellipsoids, i.e. with constant axial ratios s and q ($s < q < 1$), and that the density profile is given by

$$\rho(x, y, z) = \frac{\rho_s}{(R/R_s)^\alpha (1 + R/R_s)^{\eta-\alpha}} \quad (\text{B1})$$

$$R = \sqrt{x^2 + y^2/q^2 + z^2/s^2}$$

where ρ_s and R_s are a scale density and radius, respectively. Assuming constant axial ratios allows us to reduce the calculation of the potential to a one–dimensional integral, which in some cases can be solved analytically, after a simple transformation of the general result for ellipsoidal mass distributions (Chandrasekhar 1969).

We first consider $\eta = 3$. This was found to be a good approximation (assuming constant axial ratios) by Jing & Suto (2002) for their 12 high–resolution haloes. We also find this to be a good approximation for the haloes of two high–resolution hydrodynamical simulations we discuss in Appendix C. However, since spherical fits to large samples of haloes find deviations from this value (Avila-Reese et al. 1999; Thomas et al. 2001), we also generalize the results to other values below.

The potential of a thin homeoid of mass M (axes $a > b > c$), at a point (x, y, z) outside the shell, can be written as (Chandrasekhar 1969)

$$\Phi_M(x, y, z) = -\frac{GM}{2} \int_{\lambda}^{\infty} \frac{du}{\sqrt{(a^2+u)(b^2+u)(c^2+u)}}. \quad (\text{B2})$$

The parameter λ in equation (B2) is the parameter of the confocal ellipse passing through (x, y, z) ; it is the largest root of

$$\frac{x^2}{a^2+\lambda} + \frac{y^2}{b^2+\lambda} + \frac{z^2}{c^2+\lambda} = 1. \quad (\text{B3})$$

Since the integral (B2) can be solved analytically, we find that

$$\Phi_M(x, y, z) = -\frac{GM}{\sqrt{a^2-c^2}} \text{EllipticF} \left(\sqrt{\frac{a^2-c^2}{a^2+\lambda}}, \sqrt{\frac{a^2-b^2}{a^2-c^2}} \right) \quad (\text{B4})$$

The potential inside the homeoid is a constant (Chandrasekhar 1969), therefore it is given by $\Phi_M(x, y, z)$ with $\lambda = 0$.

We can construct the potential inside a triaxial NFW-type halo now, assuming homeoidal symmetry (i.e. constant axial ratios). First, for the potential at (x, y, z) due to all mass shells inside (i.e. inside the shell passing through the point) we find

$$\Phi_{in} = -A \zeta^{2-\alpha} \int_0^1 dm \frac{m^{1-\alpha}}{(1+m\zeta)^{3-\alpha}} \times \text{EllipticF} \left(\sqrt{\frac{1-s^2}{1+\lambda(m)/m^2 R^2}}, \sqrt{\frac{1-q^2}{1-s^2}} \right). \quad (\text{B5})$$

Here $\zeta = R/R_s$, $A = 4\pi G s q \rho_s R_s^2 / \sqrt{1-s^2}$, and $\lambda(m)$ is the largest root of

$$\frac{x^2}{m^2 R^2 + \lambda} + \frac{y^2}{m^2 R^2 q^2 + \lambda} + \frac{z^2}{m^2 R^2 s^2 + \lambda} = 1. \quad (\text{B6})$$

Second, for the potential due to all shells outside we find

$$\Phi_{out} = -\frac{A}{2-\alpha} \text{EllipticF} \left(\sqrt{1-s^2}, \sqrt{\frac{1-q^2}{1-s^2}} \right) \times \left(1 - \left(\frac{\zeta}{1+\zeta} \right)^{2-\alpha} \right). \quad (\text{B7})$$

The total potential is then $\Phi(x, y, z) = \Phi_{in} + \Phi_{out}$. Also, we find that the only change needed for $\eta \neq 3$ is to replace $(1+m\zeta)^{3-\alpha}$ by $(1+m\zeta)^{\eta-\alpha}$ in equation (B5), and to replace $(1 - (\zeta/(1+\zeta))^{2-\alpha})$ in equation (B7) by

$$\frac{(2-\alpha)\Gamma(2-\alpha)\Gamma(\eta-2)}{\Gamma(\eta-\alpha)} - \frac{\zeta^{2-\alpha} \text{hypergeom}([1, \eta-\alpha], [3-\alpha], \zeta/(1+\zeta))}{(1+\zeta)^{\eta-\alpha}}. \quad (\text{B8})$$

For spherical symmetry ($q = s = 1$) we can check the

standard result for the potential of an NFW halo. We can use $\text{EllipticF}(x, 1) = x + O(x^3)$ to get

$$\frac{1}{\sqrt{1-s^2}} \text{EllipticF} \left(\sqrt{\frac{1-s^2}{1+\lambda(m)/m^2 R^2}}, \sqrt{\frac{1-q^2}{1-s^2}} \right) = \frac{1}{\sqrt{1+\lambda(m)/m^2 R^2}}. \quad (\text{B9})$$

In this case ($q = s = 1$) the right hand side is just m , and for the NFW profile ($\alpha = 1, \eta = 3$) we have

$$\int_0^1 \frac{m dm}{(1+m\zeta)^2} = \frac{\ln(1+\zeta) + \ln(1+\zeta)\zeta - \zeta}{\zeta^2(1+\zeta)}. \quad (\text{B10})$$

Therefore, at radial distance $r = \sqrt{x^2 + y^2 + z^2}$

$$\Phi_{in}(r) = -4\pi G \rho_s R_s^2 \left(\frac{\ln(1+r/R_s)}{r/R_s} - \frac{1}{1+r/R_s} \right) \quad (\text{B11})$$

$$\Phi_{out}(r) = -4\pi G \rho_s R_s^2 \left(1 - \frac{r/R_s}{1+r/R_s} \right)$$

and the total potential takes the standard form,

$$\Phi(r) = -4\pi G \rho_s R_s^2 \frac{\ln(1+r/R_s)}{r/R_s}. \quad (\text{B12})$$

For $\alpha \neq 1$ and $\eta \neq 3$, the integral in equation (B5) can be obtained analytically. The spherical potential of a generalized NFW halo is then

$$\Phi(r) = -4\pi G \rho_s R_s^2 \left\{ \frac{\Gamma(2-\alpha)\Gamma(\eta-2)}{\Gamma(\eta-\alpha)} + \frac{(r/R_s)^{2-\alpha} \Delta(r/R_s)}{(2-\alpha)(1+r/R_s)^{\eta-\alpha}} \right\}, \quad (\text{B13})$$

where

$$\Delta(x) = \frac{2-\alpha}{3-\alpha} \text{hypergeom} \left([1, \eta-\alpha], [4-\alpha], \frac{x}{1+x} \right) - \text{hypergeom} \left([1, \eta-\alpha], [3-\alpha], \frac{x}{1+x} \right). \quad (\text{B14})$$

APPENDIX C: A COMPARISON OF X-RAY ELLIPTICITY MEASURES

Here we evaluate the reliability of our method for predicting individual cluster X-ray ellipticities based on the calculated axial ratios of dark matter haloes. Using a hydrodynamical simulation (with cooling) of a single cluster Buote & Tsai (1995) found that this method, assuming isothermal gas, allows an accurate estimation of the ellipticity of the dark matter even if the gas has a strong temperature gradient, so long as any substructure in the cluster is excluded in the analysis. We use high-resolution *adiabatic* hydrodynamical simulations of two clusters in order to calculate X-ray SB maps directly from the gas data of the simulations. We then compare these maps in detail to predictions based on the properties of their dark matter haloes, using the theoretical model described in Appendix A. We find that the theoretical

Table C1. Ellipticity results for Λ CDM cluster; see Figure C1. Here $\epsilon_X = 1 - \Lambda_-^2/\Lambda_+^2$

LOS	ϵ_X^{gas} > 0.01	ϵ_X^{model} > 0.01	ϵ_X^{gas} > 0.1	ϵ_X^{model} > 0.1	ϵ_X^{gas} 0.01 – 0.08	ϵ_X^{model} 0.01 – 0.08	ϵ_X^{gas} 0.1 – 0.2	ϵ_X^{model} 0.1 – 0.2
x-axis	0.61	0.48	0.79	0.49	0.43	0.46	0.72	0.53
y-axis	0.24	0.23	0.40	0.24	0.28	0.23	0.32	0.26
z-axis	0.65	0.51	0.77	0.53	0.51	0.50	0.69	0.48

model can work relatively well (predicting ellipticities within 10% of the gas-data values) depending on exactly how the observational ellipticity is defined. A statistical (rather than case-by-case) test of the model is presented in Section 2.

We first discuss a Λ CDM cluster that has been studied in detail by Nagai & Kravtsov (2003). In Figure C1 we show a “surface brightness” map calculated from the gas data of the simulation. The solid lines really show contours of constant value of $\int \rho_{gas}^2$, where the integration is along a LOS parallel to the x-axis of the simulation box. Of course, $SB \propto \int \rho_{gas}^2 \sqrt{T}$, but we have dropped the temperature dependence for simplicity, given that it makes only a small difference in calculated ellipticities ($\lesssim 5\%$; see below). We calculate SB for a given “pixel” by summing over all cells along the LOS. Coordinates are shown in pixels, with $7.8 h^{-1}$ kpc per pixel. The dotted-line contours are the SB contours predicted by the model described in Appendix A with the factor Γ chosen to match the radial SB profile, $\Gamma = 10.5$. For this halo $c_{vir} = 11.5$, therefore $\Gamma \sim c_{vir}$, as expected (see Section 2). The X-ray ellipticities discussed here are only mildly dependent on Γ (e.g. $\epsilon_X^{model} = 0.46$ in Table C1 changes to $\epsilon_X^{model} = 0.40(0.48)$ for $\Gamma = 8(13)$). They are mostly sensitive to the axial ratios s and q , and the relative orientation of the LOS, described by polar angles ϕ and θ in the principal-axis coordinate system. The axial ratios and polar angles were calculated inside an ellipsoid of semi-major axis $600 h^{-1}$ kpc using the iterative method described in the text, and are shown at the top of the figure. The dashed-line contour illustrates a predicted isophotal contour based on axial ratios calculated with the prescription of Kasun & Evrard (2004). The result is very similar for SZ isodecrement contours.

The highly irregular, innermost solid contour is due to a minor merger nearly in the “plane of the sky” (about 25° off the y-axis of the box). The merger is ideal to test quantitatively observational strategies to calculate an ellipticity that best represents the global triaxiality of the dark matter halo. It is also an ideal test of the reliability of our method because it allows us to gauge what bias can be introduced in the calculation of ellipticities by the presence of a minor merger, which can be expected to be common for cluster-size systems. We discuss both of these issues below.

There are various strategies to calculate X-ray ellipticities. Here we consider the method used by Kolokotronis et al. (2001) (22 clusters; ROSAT data) and McMillan et al. (1989) (49 clusters; *Einstein* data) as examples used in analyses of samples of clusters. Both studies use the method of Carter & Metcalfe (1980) adapted to an X-ray image. The ellipticity is calculated from the positive roots Λ_+ and Λ_- ($\Lambda_+ > \Lambda_-$) of the characteristic equation

$$(\mu_{20} - \Lambda^2)(\mu_{02} - \Lambda^2) = \mu_{11}^2. \quad (C1)$$

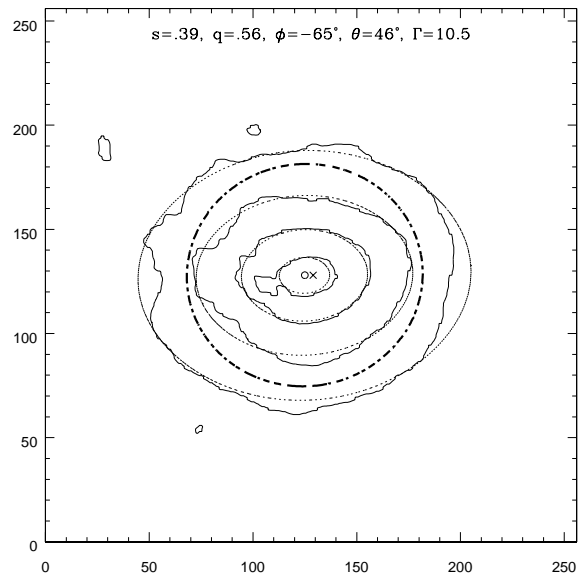


Figure C1. Surface brightness plot for the Λ CDM cluster in the yz -plane of the simulation box. The axes are in pixels ($7.8 h^{-1}$ kpc per pixel) and the solid lines show contours of constant $\int \rho_{gas}^2$, spaced by factors of 10. The SB peak (centroid) is indicated by the cross (open circle), and the innermost solid contour corresponds to a level of 15% of peak value. The dotted-line contours show the predictions of the analytic model described in Appendix A. The factor Γ is estimated by fitting, for one projection, the radial SB profile of the simulation. It is then used for all other projections. Finally, the dashed-line contour illustrates a predicted contour if a more global measure of triaxiality were used. See the text for further discussion.

The moments μ_{mn} are defined in terms of the flux f_{ij} at a given pixel (x_i, y_j) by

$$\mu_{mn} = \sum_{ij} f_{ij} (x_i - \bar{x})^m (y_j - \bar{y})^n / \sum_{ij} f_{ij}, \quad (C2)$$

where (\bar{x}, \bar{y}) is the image centroid ($\bar{x} = \sum_{ij} x_i f_{ij} / \sum_{ij} f_{ij}$, $\bar{y} = \sum_{ij} y_j f_{ij} / \sum_{ij} f_{ij}$). The ellipticity is then calculated as

$$\epsilon_X = 1 - \Lambda_-^2 / \Lambda_+^2 \quad (C3)$$

by McMillan et al. (1989), and as

$$\epsilon_X = 1 - \Lambda_- / \Lambda_+ \quad (C4)$$

by Kolokotronis et al. (2001). We shall use equation (C3)

here, except when comparing directly with the data of Kolokotronis et al. (2001).

The X-ray ellipticity ϵ_X is rather sensitive to what pixels are used to calculate it. Kolokotronis et al. (2001) use all pixels above a flux threshold (which is the average flux within a region of given radius). For example, in Figure C1 this threshold is ~ 0.01 of the peak flux within $600 h^{-1}$ kpc (which is the largest radius they use to define the threshold). In Table C1 (columns 2–5) we show results for the cluster of Figure C1 for two flux thresholds (0.01 and 0.1 of the peak flux) and for a LOS along each of the axes of the simulation box. This choice of pixels emphasizes the brightness peaks and, therefore, is more sensitive to mergers. Thus, the analytic model prediction for the ellipticity, ϵ_X^{model} , deviates significantly from the value calculated directly from the gas, ϵ_X^{gas} , except when the merger is nearly along the LOS. On the other hand, McMillan et al. (1989) explicitly exclude the centre of an image in order to characterize the global dynamics of a cluster. They use all the pixels containing 20% of the flux above a faint threshold. The latter varies substantially across the sample, but for 80% of clusters it is $\sim 0.01 - 0.2$ of the peak flux. In Table C1 (columns 6–9) we show results for two flux ranges (0.01–0.08 and 0.1–0.2) and for a LOS along each of the axes. In this case the analytic model performs much better, provided the fainter threshold is chosen low enough. If we calculate the deviation of the model ellipticity from the gas ellipticity (using a flux threshold of 0.01) for 100 random LOS we find

(1) For the McMillan et al. (1989) ellipticity the analytic model works fairly well; 2/3 of the time the model predicts the ellipticity within 10% of the gas value. Also, it would not bias a statistical sample because it predicts larger and smaller values with equal frequency.

(2) For the Kolokotronis et al. (2001) ellipticity the analytic model predicts a systematically smaller value. This is expected in this case because the model misses the merger, therefore it predicts rounder SB contours from all viewing angles. In this case we find that 2/3 of the time the value is 20 – 30% smaller.

We find similar trends for the mean and the dispersion of ellipticities calculated for the sample of clusters discussed in Section 2, although individual values can deviate more than indicated here.

The flux level at the outermost contour in Figure C1 is ~ 0.002 of the peak flux. At this flux level the contour is clearly rounder than the model prediction (due to the fact that the dark matter halo gets rounder farther out, whereas the analytic model assumes constant axial ratios). However, pixels up to much higher flux levels (~ 0.06 of peak flux) enter the calculation in order to accumulate 20% of the flux above this fainter threshold in the approach of McMillan et al. (1989). For example, for the x-axis $\epsilon_X^{gas} = 0.41$ and $\epsilon_X^{model} = 0.45$ in the flux range 0.002 – 0.06 of peak flux. Therefore, the model works well down to lower thresholds.

The analytic model assumes that the gas is isothermal in order to predict the SB. We can check how much this is likely to affect a comparison with actual data by calculating the ellipticity from the simulation data including the temperature dependence. We find that for the flux levels considered here, the effect is rather small. For example, the entry in column 2 of Table C1 would be 0.59 (0.23, 0.63) for

the x-axis (y-axis, z-axis) as compared to 0.61 (0.24, 0.65) assuming isothermality. The temperature in this cluster falls by a factor ~ 1.9 in the radial range $(0.1 - 0.5)r_{vir}$, which is consistent with observations (see De Grandi & Molendi 2002, and references therein). Therefore, the temperature variation of the simulation gas is representative of that of real clusters.

We have also tested whether using the dark matter potential of this cluster directly would significantly improve the prediction for ϵ_X . The assumptions are still the same, but the potential is calculated directly from the dark matter distribution in order to predict the gas density. We find that the results improve as follows. For example, the entry in column 3 of Table C1 would be 0.53 (0.25, 0.55) for the x-axis (y-axis, z-axis) instead of 0.48 (0.23, 0.51).

Finally, in order to study whether the analytic model indeed performs better in the absence of a merger, we have analysed in the same manner a high-resolution simulation cluster that does not have an ongoing merger. It is a SCDM cluster discussed in detail by Kravtsov et al. (2002). In Figure C2 we show the SB map calculated as in Figure C1, and in Table C2 we show the results for the ellipticity. For this cluster $\Gamma = 9.3$ and $c_{vir} = 10.4$, therefore $\Gamma \sim c_{vir}$ as before. In this case the model works reasonably well for either one of the definitions of ellipticity, provided that the flux threshold is sufficiently high. For faint thresholds the model fails to reproduce the trend of rounder and twisted SB contours in the simulation (for LOS = y-axis, the reverse trend in Table C2 is due to the chance projection of a distant hot spot that appears only at a level ~ 0.01 of peak flux). It is in fact the twisted SB contours that cause most of the difference between model and simulation gas. This is due to the fact that isodensity shells are fairly misaligned in this case. The projected, $100 h^{-1}$ kpc-thick isodensity shell of $400 h^{-1}$ kpc ($800 - 900 h^{-1}$ kpc, $1000 - 1050 h^{-1}$ kpc) semi-major axis makes a 15° (35° , 60°) angle with the vertical direction in Figure C2. Such large misalignments were found to be rare by Jing & Suto (2002), therefore we assume here that the model also works down to the faint threshold level of ~ 0.01 of peak flux in the absence of a merger, and for both ellipticities.

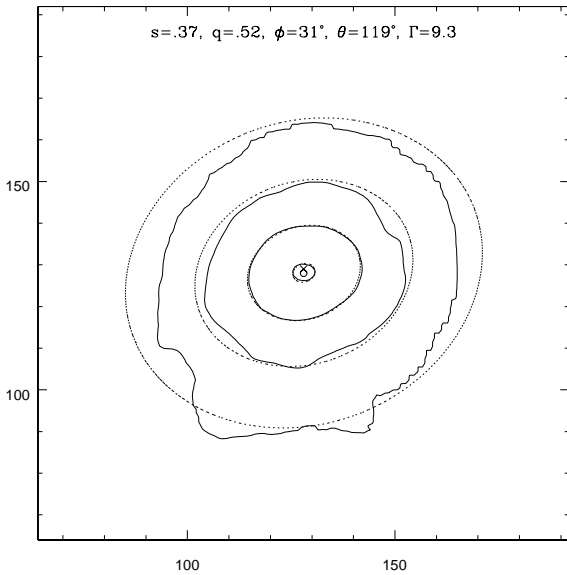
In Section 3 we analyse the expected distribution of X-ray ellipticities for cluster-mass haloes in the cosmological box discussed in Section 2. We calculate ellipticities using the analytic model, and compare the distribution to the data of McMillan et al. (1989) and Kolokotronis et al. (2001).

We have also considered the reliability of the analytic model to predict the shape of SZE maps of clusters. In Figure C3 we show “temperature decrement” maps for the two clusters we have discussed. The solid lines show contours of constant value of $\int \rho_{gas} T$ (spaced by factors of 3). The integration is along a LOS parallel to the x-axis of the corresponding simulation box, as was the case in Figures C1 and C2. Since the dependence on gas temperature is linear in this case, we can expect a more significant effect of temperature on the shape of isodecrement contours. The top panels of Figure C3 compare the shape of the contours of constant value of $\int \rho_{gas}$ only (dashed lines) to decrement contours.³

³ The dashed-line contours are not shown spaced by a fixed factor. The levels are just chosen to give contours of similar size to

Table C2. Ellipticity results for SCDM cluster; see Figure C2. Here $\epsilon_X = 1 - \Lambda_-^2 / \Lambda_+^2$

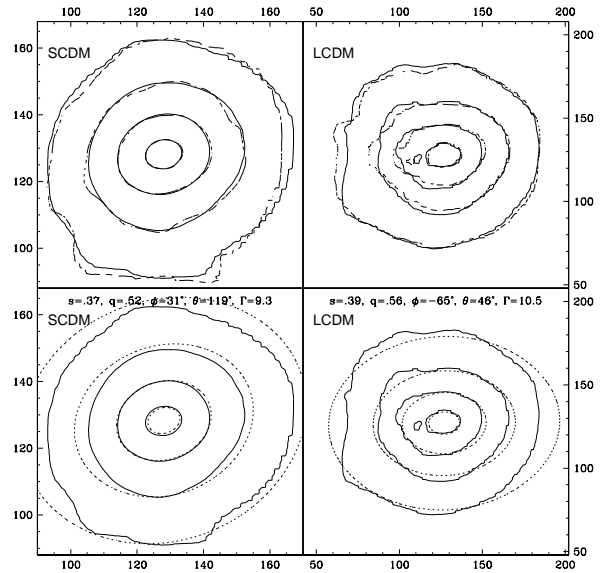
LOS	ϵ_X^{gas} > 0.01	ϵ_X^{model} > 0.01	ϵ_X^{gas} > 0.1	ϵ_X^{model} > 0.1	ϵ_X^{gas} 0.01 – 0.09	ϵ_X^{model} 0.01 – 0.09	ϵ_X^{gas} 0.1 – 0.2	ϵ_X^{model} 0.1 – 0.2
x-axis	0.30	0.35	0.38	0.38	0.25	0.34	0.38	0.34
y-axis	0.48	0.37	0.45	0.42	0.51	0.35	0.42	0.39
z-axis	0.48	0.55	0.52	0.56	0.44	0.54	0.48	0.55


Figure C2. Surface brightness plot for the SCDM cluster in the yz -plane of the simulation box. The axes are in pixels ($15.6 h^{-1}$ kpc per pixel) and the meaning of symbols is as in Figure C1. In this case the innermost solid contour corresponds to a level of 25% of peak value, and each solid contour is drawn at one tenth of the solid-contour levels of Figure C1.

Both sets of solid contours are calculated directly from the gas and temperature data of the corresponding simulation. It can be seen that in the presence of a merger (the Λ CDM cluster case) the temperature dependence indeed makes the isodecrement contours noticeably different from contours of $\int \rho_{gas}$. However, in the absence of a merger (the SCDM cluster case) they agree fairly well in shape. For example, the ellipticity $\epsilon_{SZE} = 1 - \Lambda_-^2 / \Lambda_+^2$, calculated using the signal between the second and third contours, is $\epsilon_{SZE} = 0.20$ (0.24) for the SCDM (Λ CDM) cluster. The ellipticities calculated using the gas density alone are 0.21 and 0.36, respectively. Thus, analytic models to calculate ϵ_{SZE} assuming isothermal gas will err by a large margin in the presence of a merger, *even if ϵ_{SZE} is calculated outside the core region*. This is unlike what we have found for X-ray ellipticities.

Furthermore, even in the absence of a merger, the changing triaxiality of the dark matter halo makes model predictions for ellipticity in the SZ maps miss the values

the solid contours, in order to compare shapes at a given radial distance.


Figure C3. Temperature decrement map for the two clusters of Figures C1 and C2, in the yz -plane of the corresponding simulation boxes. The axes are in pixels, and each box is $1.25 h^{-1}$ Mpc across. The solid lines show contours of constant $\int \rho_{gas} T$, spaced by factors of 3. The innermost solid contour corresponds to a level of 60% (50%) of peak value for the SCDM (Λ CDM) cluster. The top panels compare the shape of the contours of constant $\int \rho_{gas}$ (dashed lines) to the decrement-level contours. The bottom panels compare the prediction of the analytic model for $\int \rho_{gas}$ (dotted lines) with the decrement-level contours. See the text for further discussion.

ϵ_{SZE} by a larger margin than in the case of X-ray ellipticity. The bottom panels of Figure C3 show the predictions of the analytic model for $\int \rho_{gas}$ (dotted lines) compared to the “isodecrement contours” of the top panels (solid lines). It can be seen there that, even in the absence of a merger (left), the ellipticity of the analytic model contours is too large (even if compared to the simulation-data contours for $\int \rho_{gas}$ only (dashed-lines of top panels)). For example, the ellipticity between the second and third contours of the analytic model predictions is 0.33 (0.46) for the SCDM (Λ CDM) cluster. We find similar results for the other LOS. Thus, reliable predictions (i.e. within 10% of gas-data values) for ellipticity in SZE maps need to incorporate the changing triaxiality of the dark matter haloes. However, the model is still useful to predict statistics of cluster samples such as the mean and dispersion. See Section 2.

REFERENCES

- Allgood, B., Flores, R. A., Primack, J. R., Kravtsov, A. V., Wechsler, R. H., Faltenbacher, A., & Bullock, J. S. 2005, preprint (astro-ph/0508497)
- Avila-Reese, V., Firmani, C., Klypin, A.A., & Kravtsov, A.V. 1999, MNRAS 310, 527
- Barnes, J., & Efstathiou, G. 1987, ApJ 319, 575
- Binney, J. 1985, MNRAS, 212, 767
- Bryan, G. L., & Norman, M. 1998, ApJ 495, 80
- Bullock, J. S. 2002, Proceedings of the Yale Cosmology Workshop, The Shapes of Galaxies and Their Dark Matter Halos, ed. P. Natarajan Singapore: World Scientific, 109
- Buote, D. A. & Tsai, J. C. 1995, ApJ 439, 29
- Buote, D. A., Hart, B. C., & Humphrey, P. J. 2005, to be submitted to ApJ.
- Buote, D. A., & Canizares, C. R. 1996, ApJ 457, 565
- Carlstrom, J. E., Holder, G. P., & Reese, E. D. 2002, ARA&A, 40, 643
- Carter, D., & Metcalfe, N. 1980, MNRAS, 191, 325
- Chandrasekhar, S. 1969, Ellipsoidal Figures of Equilibrium New Haven: Yale University Press
- De Grandi, S. & Molendi, S. 2002, ApJ, 567, 163
- Dubinski, J., & Carlberg, R. G. 1991, ApJ, 378, 496
- Floor, S. N., Melott, A. L., Miller, C. J., & Bryan, G. L. 2003, ApJ, 591, 741
- Floor, S. N., Melott, A. L., & Motl, P. M. 2003b, ApJ, 611, 153
- Frenk, C., White, S. D. M., Davis, M., & Efstathiou, G. 1988, ApJ 327, 507
- Hernquist, L. 1990, ApJ, 356, 359
- Jeltema, T. E., Canizares, C. R., Bautz, M. W., & Buote, D. A. 2005, ApJ 624, 606
- Jing, Y. P., & Suto, Y. 2002, ApJ, 574, 538
- Jing, Y. P., Mo, H. J., Borner, G., & Fang, L. Z. 1995, MNRAS, 276, 417
- Kasun, S. F., & Evrard, A. E. 2004, preprint astro-ph/0408056
- Kazantzidis, S., Kravtsov, A. V., Zentner, A. R., Allgood, B., Nagai, D., & Moore, B. 2004, ApJ, 611, L73
- Kolokotronis, V., Basilakos, S., Plionis, M., & Georgantopoulos, I. 2001, MNRAS, 320, 49
- Kravtsov, A. V., Klypin, A., & Hoffman, Y. 2002, ApJ, 571, 563
- Lee, J., & Suto, Y. 2003, ApJ, 585, 151
- McMillan, S. L. W., Kowalski, M. P., & Ulmer, M. P. 1989, ApJs, 70, 723
- Melott, A. L., Chambers, S. W., & Miller, C. J. 2001, ApJ, 559, L75
- Mohr, J. J., Evrard, A. E., Fabricant D. G., & Geller, M. J. 1995, ApJ, 447, 8
- Nagai, D., & Kravtsov, A. V. 2003, ApJ, 587, 514
- Navarro, J. F., Frenk, C. S., & White, S. D. M. 1996, ApJ, 462, 563
- Plionis, M. 2002, ApJ, 572, L67
- Reiprich, H. T., & Böhringer, H. 2002, ApJ, 567, 716
- Rosati, P., Borgani, S., & Norman, C. 2002, ARA&A, 40, 539
- Spergel, D. N., et al. 2003, ApJs, 148, 175
- Springel, V., White, S. D. M., & Hernquist, L. 2004, in IAU Symposium 220, Dark Matter in Galaxies, eds. S. Ryder, D.J. Pisano, M. Walker, & K.C. Freeman San Francisco: ASP
- Sunyaev, R. A., & Zel'dovich, Ya. B. 1970, Comments Astrophys. Space Phys., 2, 66
- Suwa, T., Habe, A., Yoshikawa, T., Okamoto, T. 2003, ApJ, 588, 7
- Thomas, P. A. et al 1998, MNRAS, 296, 1061
- Thomas, P. A. et al 2001, MNRAS, 324, 450
- Vikhlinin, A., Markevitch, M., Murray, S. S., Jones, C., Forman, W., & Van Speybroeck, L. 2005a ApJ in press (astro-ph/0412306)
- Vikhlinin, A., Kravtsov, A. V., Forman, W., Jones, C., Markevitch, M., Murray, S. S., & Van Speybroeck, L. 2005b (astro-ph/0507092)
- Wang, Y.-G., & Fan, Z.-H. 2004, ApJ, 617, 847
- Warren, M. S., Quinn, P. J., Salmon, J. K., & Zurek, W. H. 1992, ApJ, 399, 405
- Wechsler, R. H., Bullock, J. S., Primack, J. R., Kravtsov, A. V., & Dekel, A. 2002, ApJ, 568, 52